MoS2-coated vertical graphene nanosheet for high-performance rechargeable lithium-ion batteries and hydrogen production

Wang, Ye; Chen, Bo; Seo, Dong Han; Han, Zhao Jun; Wong, Jen It; Ostrikov, Kostya; Zhang, Hua; Yang, Hui Ying

2016

https://hdl.handle.net/10356/89924

https://doi.org/10.1038/am.2016.44

ORIGINAL ARTICLE

MoS$_2$-coated vertical graphene nanosheet for high-performance rechargeable lithium-ion batteries and hydrogen production

Ye Wang[1], Bo Chen[2], Dong Han Seo[3], Zhao Jun Han[3], Jen It Wong[1], Kostya (Ken) Ostrikov[3,4,5], Hua Zhang[2] and Hui Ying Yang[1]

Hybrid nanostructures composed of vertical graphene nanosheet (VGNS) and MoS$_2$ nano-leaves are synthesized by the chemical vapor deposition method followed by a solvothermal process. The unique three-dimensional nanostructures of MoS$_2$/VGNS arranged in a vertically aligned manner can be easily constructed on various substrates, including Ni foam and graphite paper. Compared with MoS$_2$/carbon black, MoS$_2$/VGNS nanocomposites grown on Ni foam exhibit enhanced electrochemical performance as the anode material of lithium-ion batteries, delivering a specific capacity of 1277 mAh g^{-1} at a current density of 100 mA g^{-1} and a high first-cycle coulombic efficiency of 76.6%. Moreover, the MoS$_2$/VGNS nanostructures also retain a capacity of 1109 mAh g^{-1} after 100 cycles at a current density of 200 mA g^{-1}, suggesting excellent cycling stability. In addition, when the MoS$_2$/VGNS nanocomposites grown on graphite paper are applied in the hydrogen evolution reaction, a small Tafel slope of 41.3 mV dec^{-1} and a large double-layer capacitance of 7.96 mF cm^{-2} are obtained, which are among the best values achievable by MoS$_2$-based hybrid structures. These results demonstrate the potential applications of MoS$_2$/VGNS hybrid materials for energy conversion and storage and may open up a new avenue for the development of vertically aligned, multifunctional nanoarchitectures.

INTRODUCTION

Two-dimensional materials such as graphene and transition metal dichalcogenides have recently attracted tremendous research interest owing to their unique physical, chemical and mechanical properties. MoS$_2$, a newly discovered bandgap-adjustable semiconductor, has a typical layered structure composed of three S-Mo-S atomic layers stacked together through weak van der Waals interactions.[1,2] Owing to its structural, electronic and electrochemical features, MoS$_2$ has been explored as the active material for various devices, including field-effect transistors,[3] light-emitting diodes,[4] biosensors,[5] lithium-ion batteries (LIBs) and hydrogen production.[6–10]

MoS$_2$ shows a number of advantageous features when used as the anode of LIBs. First, MoS$_2$ has a theoretical specific capacity of ~ 670 mAh g^{-1}, which is almost double the capacity of graphite, the dominant anode material of current commercial LIBs.[1] Second, the layered structure and weak van der Waals interactions can enable the lithium ions to easily access the interlayer spacing of MoS$_2$, leading to a fast lithiation/delithiation process without a significant volume change.[11] Indeed, the volume expansion of MoS$_2$ during the lithiation and delithiation processes is only 103%, which is much lower than

that of other alloying–dealloying and/or conversion-based anode materials (for example, silicon has 280% of volume expansion upon lithiation).[11] The stable structure of MoS$_2$ thus prevents the common pulverization problem observed in charge storage devices.[12] Nevertheless, the drawbacks of large irreversible capacity in the first cycle, fast capacity fading and inferior rate capability have thus far impeded the widespread application of MoS$_2$-based anodes of LIBs.[8]

MoS$_2$ has also received increasing interest as the catalyst in hydrogen evolution reaction (HER) owing to its chemical stability, relatively low cost and high photocatalytic/electrocatalytic property.[13] It has been reported that the electrocatalytic activity originates from the sulfur edges of MoS$_2$ layers, and the inner planes are catalytically inert.[6] However, the development of MoS$_2$ electrocatalyst is still in its infantry owing to challenges such as low conductivity and inherent stacking of MoS$_2$ sheets.[14]

To resolve these issues, various carbonaceous materials, including carbon nanotubes, activated carbon and graphene, have been employed to support the MoS$_2$ nanostructures.[6,12] These conductive hosts not only improve electronic conductivity but also reduce lithium-ion diffusion length and increase the electrochemical and

[1]Pillar of Engineering Product Development, Singapore University of Technology and Design, Singapore, Singapore; [2]Center for Programmable Materials, School of Materials Science and Engineering, Nanyang Technological University, Singapore, Singapore; [3]CSIRO Manufacturing, Lindfield, NSW, Australia; [4]School of Chemistry, Physics and Mechanical Engineering, Queensland University of Technology, Brisbane, Queensland, Australia and [5]School of Physics, The University of Sydney, Sydney, NSW, Australia
Correspondence: Professor HY Yang, Pillar of Engineering Product Development, Singapore University of Technology and Design, 8 Somapah Road, Singapore 487372, Singapore.
E-mail: yanghuiying@sutd.edu.sg

2

electrocatalytic efficiency of the MoS$_2$ nanostructure.[12] For example, MoS$_2$/graphene nanocomposites,[15] hierarchical MoS$_x$/carbon nanotube nanocomposites,[1] MoS$_2$/three-dimensional graphene (3D) networks,[16] and honeycomb-like MoS$_2$ on 3D graphene foam were reported to have a high reversible capacity and long cycle stability for LIBs.[8] Reduced graphene oxide, carbon sponge and 3D graphene were also used to support MoS$_2$ to enhance the HER efficiency by increasing the charge transfer mobility and exposing more sulfur edge active sites.[6,13,17] In particular, carbonaceous hosts constructed in a 3D architecture can provide an ideal platform with a large surface area and free volume for electrolyte flow and hydrogen escape that are desirable in the LIB and HER processes.[17] However, the available surface area for MoS$_2$ loading in the present 3D conductive hosts remains low owing to the intrinsic flat surface at the microscopic scale (for example, horizontal graphene), thereby limiting the performance of rate capability, energy and power densities and catalytic activity.[13] In addition, most electrodes require polymeric adhesives to bind the active materials, further complicating the electrode fabrication process and increasing the cost.

In this work, we demonstrate vertical graphene nanosheet (VGNS) as an effective platform for the loading of MoS$_2$ without additional conductive agents and binders.[18,19] VGNS consists of few-layered graphene sheets self-organized in a vertical orientation with an inherently open and interconnected array structure. The structural rigidity of VGNS can prevent the restacking of graphene nanosheets, a commonly observed problem in horizontal graphene.[20–22] Using a simple solvothermal method, we further show that MoS$_2$ nano-leaves with a thickness of ∼ 3 nm can be directly grown on VGNS with a controllable mass loading and pore size distribution. This unique nanoarchitecture design offers several attributes for effective energy storage and conversion. First, MoS$_2$ nano-leaves firmly grow on the surface of VGNS, which not only act as the growth backbone for MoS$_2$ nano-leaves but also provide outstanding electronic conductivity to improve the electron transfer rate. Second, the vertically aligned VGNS's rigid nanostructure could effectively inhibit the MoS$_2$ restacking issue and mechanical failure during cycling testing, leading to stable performance for energy storage and conversion evaluation. Third, the ultrathin-layered structure of MoS$_2$ nano-leaves, which provide large surface area and defect sites, can effectively enhance the ion accessibility and reduce the ion diffusion length. Owing to these advantages, the resultant binder-free MoS$_2$/VGNS hybrid electrodes exhibit excellent specific capacity, rate capability and cycling stability for LIBs and greatly improve the electrocatalytic efficiency in HER-related applications. Our results demonstrate the importance of optimal nanostructure design in the MoS$_2$/VGNS nanocomposites for energy conversion and storage devices, which may shed light on addressing the challenges in a variety of functional materials and advanced applications.

EXPERIMENTAL PROCEDURES
Preparation of MoS$_2$/VGNS structure
According to different requirements for LIBs and hydrogen production evaluation, MoS$_2$/VGNS was grown on Ni foam and graphite paper, respectively. Material synthesis can be divided into two steps: VGNS grown on Ni foam or graphite paper followed by MoS$_2$ synthesized on VGNS. Specifically, VGNS was first grown in a plasma-assisted chemical vapor deposition (CVD) process by using butter as the solid precursor.[18] MoS$_2$/VGNS nanocomposites were then synthesized via a simple solvothermal method.[1] Various amounts of (NH$_4$)$_2$MoS$_4$ powder (3, 11 and 22 mg for LIB experiments and 11, 22, 55 and 110 mg for HER experiments) were dispersed into 30 ml *N,N*-dimethylformamide (DMF) by ultrasonication and

continuously stirred for approximately 15 min at room temperature. After that, a piece of VGNS (2 × 1 cm) was immersed in the solution and transferred to a 50-ml Teflon-lined stainless steel autoclave, sealed and kept in a laboratory oven at 200 °C for 10 h for solvothermal reaction. The product was then washed by deionized water several times to remove the residual chemicals. After drying the product at 100 °C overnight in a vacuum oven, the final samples were obtained by annealing at 200 °C (on Ni foam) or 120 °C (on graphite paper) for 2 h in the H$_2$/N$_2$ (5%/95%) gas flow to remove the sulfur residue and improve the MoS$_2$ crystallinity. For the LIB tests, an MoS$_2$/carbon black (MoS$_2$/CB) control sample was also prepared by dissolving 10 mg of CB and 220 mg of (NH$_4$)$_2$MoS$_4$ powder into 30 ml of DMF. The same solvothermal and postannealing conditions were applied as that of the MoS$_2$/VGNS sample.

Material characterization
The morphology and structure of the synthesized nanostructures were measured by field-emission scanning electron microscopy (SEM; JSM-7600F, JEOL, Tokyo, Japan) and transmission electron microscopy (TEM; JEM-2100F, JEOL). Energy-dispersive X-ray (EDX) analysis was carried out in SEM JSM-7600F, JEOL, equipped with an EDX module (X-Max^N, Oxford Instruments, Oxfordshire, UK). Raman spectra were obtained by a confocal Raman system with laser excitation at 532 nm (WITec Instruments Corp., Ulm, Germany).

Battery assembly and electrochemical measurements
The electrochemical performance of MoS$_2$/VGNS nanocomposites was measured by assembling them into a half-cell testing configuration based on the CR2032 coin cell, where the active material without any additive or binder was used as the working electrode, a lithium foil as the counter electrode and a Celgard 2400 membrane as the separator. The MoS$_2$/VGNS nanocomposite was directly used as the working electrode without pressing into slices to avoid peeling off from the current collector. One molar LiPF$_6$ solution in a 1:1 (v:v) mixture of ethylene carbonate/dimethyl carbonate was employed as the electrolyte to fill into the coin cell. For the fabrication of the MoS$_2$/CB electrode, MoS$_2$/CB nanocomposite was mixed with the conductive CB and polyvinylidene fluoride binder at a weight ratio of 80:10:10 and added with several drops of *N*-methyl pyrrolidone solution to form a slurry. The slurry was then coated onto Ni foam and dried in a vacuum oven at 120 °C overnight. All components listed above were assembled into a standard CR2032 coin cell in a glove box filled with argon gas. Electrochemical measurements were carried out after 24 h of battery assembly. The cyclic voltammetric (CV) and electrochemical impedance spectroscopic (EIS) measurements were performed by an electrochemical workstation (VMP3, Bio-Logic, Claix, France). The galvanostatic charge/discharge test was measured in the voltage range of 0.01–3 V at various current densities ranging from 100 to 2000 mA g^{-1} using a battery analyzer (Neware, Shenzhen, China). The capacity of the MoS$_2$/VNGS electrode was calculated based on both MoS$_2$ and VGNS active materials, where the density of VGNS was approximately 0.3 mg cm^{-2}, and the loading of MoS$_2$ was measured by a balance (AUW120D, Shimadzu, Kyoto, Japan). The coulombic efficiency (CE) was calculated by CE = delithiation capacity/lithiation capacity × 100% = charge capacity/discharge capacity × 100%.[23]

Electrocatalytic characterization
Electrocatalytic measurements were carried out by an Autolab PGSTAT302N electrochemical workstation (Metrohm Autolab, KM Utrecht, Netherlands) with a standard three-electrode setup in a 0.5 M H$_2$SO$_4$ solution. The samples (VGNS, MoS$_2$/VGNS, MoS$_2$/CB, MoS$_2$/CB mixed with VGNS), Pt wire and 3 M Ag/AgCl electrode were used as the working electrode, counter electrode and reference electrode, respectively. All potentials were converted to values with reference to a reversible hydrogen electrode (RHE). The MoS$_2$/CB electrode was prepared by drop-casting MoS$_2$/CB suspension onto a glassy carbon electrode (5 mm in diameter). Other electrodes were used directly as the working electrode. The electrode area of these three electrodes was fixed at 0.20 cm^2 by using an electrochemically inert polyimide tape. Linear sweep voltammetry was measured at a rate of 2 mV s^{-1}. EIS was carried out at open circuit voltage with an AC signal amplitude of 5 mV in the frequency range of 100 kHz to 0.1 Hz. Cycle stability was performed continuously for 1000 cycles

between 0 and -0.3 V vs RHE at a scan rate of 100 mV s^{-1}. Prior to measurement, the solution was bubbled with nitrogen gas for 30 min to remove dissolved oxygen.

RESULTS AND DISCUSSION

Morphology and structure of the MoS$_2$/VGNS nanostructures

The growth process of MoS$_2$/VGNS nanoarchitectures is schematically illustrated in Supplementary Figure S1. First, VGNS was obtained in a plasma-assisted CVD transformation process by using butter as the solid state precursor, where the strong plasma–surface interactions can effectively break down carbon-containing molecules in butter and reconstruct them into vertically aligned graphene nanosheets.[18] The use of butter as the carbon precursor instead of hydrocarbon gases such as CH$_4$ also enabled complete coverage of VGNS on various substrates at a high mass loading.[24] After immersing VGNS into the solution of Mo salt precursor of (NH$_4$)$_2$MoS$_4$ dissolved in DMF, Mo and S ions started to nucleate on the surface of graphene nanosheets in a solvothermal process. These nucleated seeds then grew larger and expanded along the (002) direction because it has the lowest energy at the given growth temperature (200 °C).[1,8] After several hours, MoS$_2$/VGNS hybrid nanoarchitectures were formed, and the final product was obtained by removing the residual sulfur via thermal annealing under N$_2$/H$_2$ (95%/5%) atmosphere.

Figure 1 shows the morphology of pristine VGNS and MoS$_2$/VGNS grown on Ni foam. Pristine VGNS was observed to uniformly cover the skeleton of Ni foam that had submillimeter scale voids (Figure 1a), whereas cavities at the submicron scale were formed between neighboring graphene nanosheets arising from the vertical orientation of interconnected VGNS (Figure 1b).[18] Moreover, the maze-like networks of graphene nanosheets were easily distinguishable in the high-magnification SEM image (inset of Figure 1b). The height of the graphene nanosheets was ~2 μm, as illustrated by the cross-sectional SEM image in Figure 1c. This vertically aligned structure can provide good mechanical rigidity to VGNS, which effectively prevents the aggregation of graphene nanosheets for further applications, in contrast to the conventional horizontal graphenes.[25]

After growing MoS$_2$, the original macroscopic structure of VGNS on Ni foam was preserved, as shown in Figure 1d. At the microscopic scale, however, the grown MoS$_2$ was observed to fully cover the graphene nanosheets and formed a structure of nano-leaves with additional nanoscale pores (Figure 1e). The MoS$_2$ nano-leaves ramified from the VGNS backbones were clearly seen in the high-resolution SEM image (inset of Figure 1e) and can also be identified from the cross-sectional SEM image (Figure 1f), where no significant change in the height of the original VGNS was observed. This unique 3D multiscale hybrid structure of MoS$_2$/VGNS nanocomposites, constructed by the submillimeter voids of Ni foam, the submicron cavities of VGNS (Figure 1b) and the nanometer-sized porous MoS$_2$ nanoarchitectures (Figure 1e), may significantly enlarge the effective surface area for ion accessibility and facilitate ion transport by reducing the ion diffusion length.[26] In addition, EDX analysis was carried out to map the elemental distribution in the nanocomposites (Supplementary Figure S2). It was found that the peak intensity ratio of C (0.28 keV) to Mo/S (2.32 keV) at the top, middle and bottom parts of nanocomposites were 0.23, 0.22 and 0.20, respectively, demonstrating that MoS$_2$ nano-leaves were uniformly grown along the depth of VGNS. These results clearly indicated that MoS$_2$ was effectively loaded on the graphene nanosheets and adhered to the Ni foam current collector without the use of any polymeric binders.

The morphology of various loading of MoS$_2$ on VGNS by changing the amount of Mo salt precursor from 3 to 22 mg is also given in Supplementary Figure S3. In all cases, MoS$_2$ nano-leaves grew along the surface of graphene nanosheets (Supplementary Figures S3b and d). However, with the increase of Mo salt precursors, the size of MoS$_2$ nano-leaves increased, thus possibly blocking the submicron cavities of the VGNS structure (Supplementary Figure S3c). Moreover, some nano-urchin-shaped MoS$_2$ clusters were observed on the top surface in the condition of a high amount of Mo salt precursor (Supplementary Figure S3d). The mass loading of MoS$_2$ was measured to be 0.19, 1.72 and 5.04 mg cm^{-2} when the precursor was 3, 11 and 22 mg, respectively. MoS$_2$ was also grown with CB as a control sample, that is, the MoS$_2$/CB nanocomposite. The morphology of MoS$_2$/CB
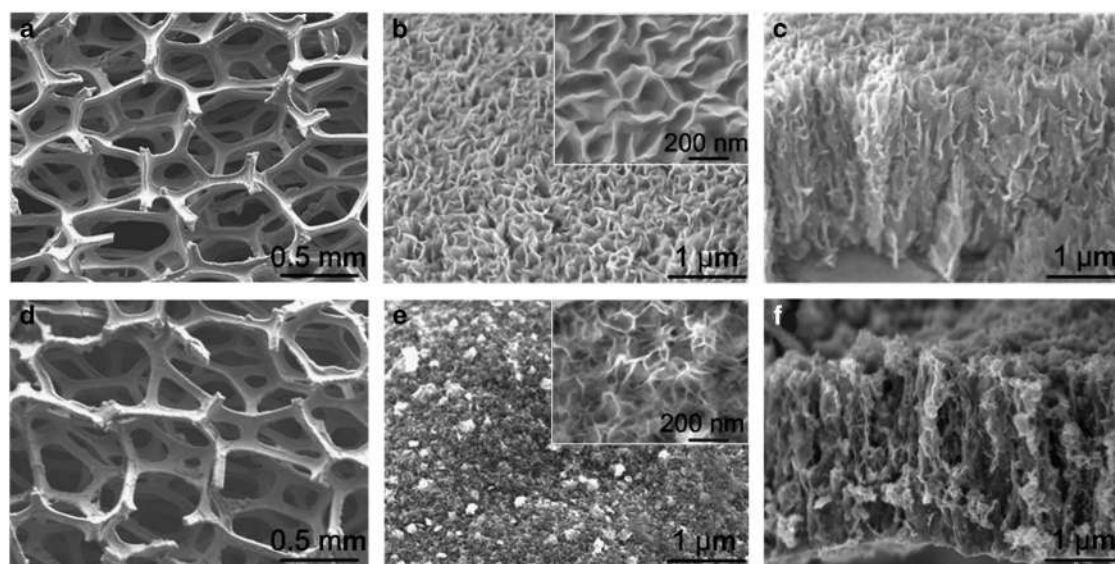
Figure 1 (**a**) Low- and (**b**) high-magnification SEM images of VGNS grown on Ni foam. Inset in (**b**) is the enlarged top view of VGNS. (**c**) Cross-sectional SEM image of VGNS. (**d**) Low- and (**e**) high-magnification SEM images of MoS$_2$/VGNS grown on Ni foam. Inset in (**e**) is the enlarged top view of MoS$_2$/VGNS. (**f**) Cross-sectional SEM image of MoS$_2$/VGNS. MoS$_2$ was grown with 11 mg of Mo salt precursor.
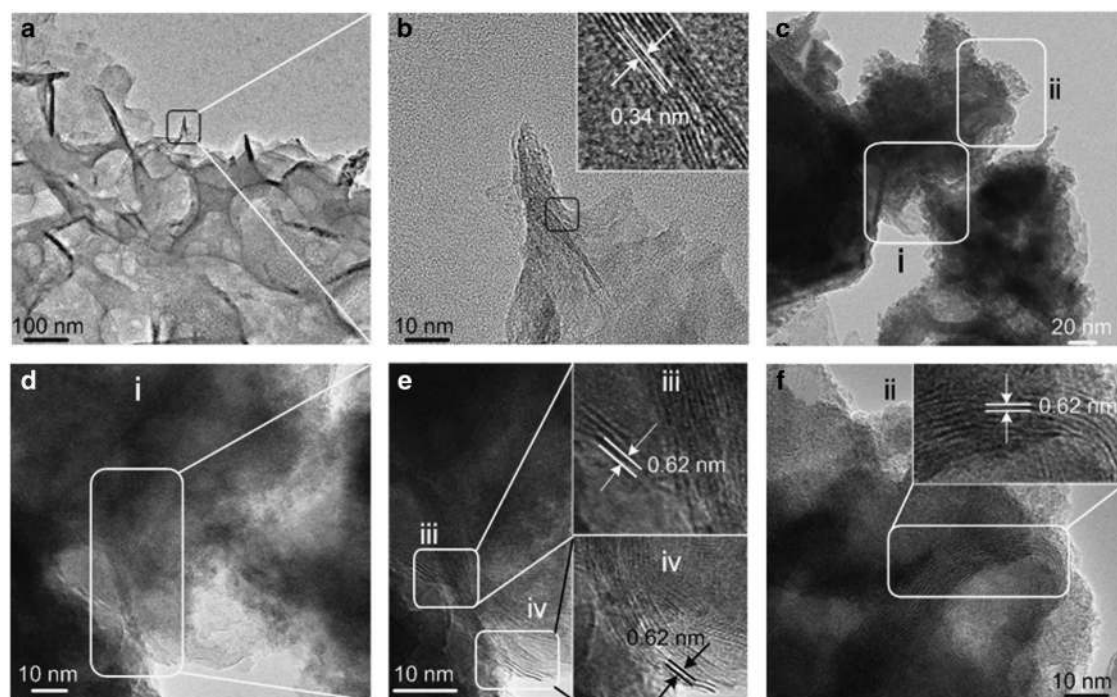
Figure 2 (**a**) TEM and (**b**) HRTEM images of pristine VGNS. Inset in (**b**) is the enlarged view of the squared area in (**b**). (**c**) TEM and (**d–f**) HRTEM images of MoS$_2$/VGNS nanocomposites. Enlarged views of the squared areas (i) to (iv) in these images are also shown. MoS$_2$ was grown with 11 mg of Mo salt precursor.

was significantly different from that of the MoS$_2$/VGNS, where aggregates of nano-urchin-shaped MoS$_2$ clustered in random sizes were ubiquitously observed (Supplementary Figure S4).

Figures 2a and b show the typical TEM images of pristine VGNS. A closer inspection of the high-resolution TEM (HRTEM) image shows that the graphene nanosheets were composed of 5–7 graphene layers with an inter-planar spacing of 0.34 nm, corresponding to the (002) crystal plane of graphite (inset of Figure 2b).[18] TEM and HRTEM images of MoS$_2$/VGNS grown on Ni foam are shown in Figures 2c–f. It was observed that, after the growth of MoS$_2$ nano-leaves, the nanosheets became much darker under the electron beam of TEM (Figure 2c), suggesting the coverage of MoS$_2$ on the graphene nanosheets. The MoS$_2$ nano-leaves showed a typical size of approximately 50 nm. HRTEM images also indicated that individual MoS$_2$ nano-leaves were composed of 2–6 layers with an inter-planar spacing of 0.62 nm (insets of Figures 2e and f), corresponding to the (002) crystal plane of MoS$_2$.[12,27]

Raman spectra of the pristine VGNS, MoS$_2$/VGNS and MoS$_2$/CB are shown in Supplementary Figure S5. Two characteristic Raman peaks in Supplementary Figure S5a located at 382 and 408 cm^{-1} can be assigned to the typical Raman active E$_{2g}^1$ and A$_{1g}$ modes of MoS$_2$, respectively.[28] A weak peak located at ~ 450 cm^{-1} can be attributed to the 2LA(M) mode of MoS$_2$.[29] The peaks in Supplementary Figure S5b located at 1351 and 1589 cm^{-1} are attributed to the D and G bands of VGNS, corresponding to the disorder carbon atoms in the hexagonal graphitic network and the in-plane vibrational mode of sp^2-bonded carbon atoms, respectively.[30,31] It was found that the D and G peaks were much weaker in the MoS$_2$/VGNS nanocomposites compared with the pristine VGNS, implying the coverage of MoS$_2$ nano-leaves on the graphene nanosheets.
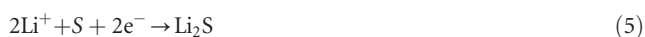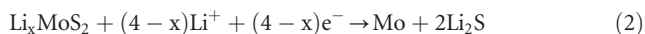
Lithium-ion storage performance

The lithium-ion storage performance of MoS$_2$/VGNS nanocomposites grown on Ni foam was first evaluated in a half-cell battery configuration. Coin-type cells were assembled with MoS$_2$/VGNS as the working electrode, lithium foil as the counter electrode and Celgard 2400 membrane as the separator. Figure 3a shows the CV curve of MoS$_2$/VGNS grown with 11 mg of Mo salt precursor. The first three cycles in the potential range of 0.01–3 V (vs Li/Li$^+$) were plotted at a scan rate of 0.1 mV s^{-1}. The CV shape of MoS$_2$/VGNS hybrid was drastically different from that of pure VGNS (Supplementary Figure S6a) but was similar to that of MoS$_2$/CB (Supplementary Figure S7a), suggesting that the lithiation/delithiation process was mainly contributed by MoS$_2$. The possible process/ mechanism is proposed to be divided into the following steps. Specifically, there were two peaks centered at 1.0 and 0.5 V in the first cathodic scan. The former was related to the lithium ions intercalated into the MoS$_2$ layered structure to form Li$_x$MoS$_2$ (Equation 1),[1] whereas the latter was associated with the decomposition of Li$_x$MoS$_2$ into metallic Mo nanoparticles and amorphous Li$_2$S (Equation 2) and the formation of a gel-like solid electrolyte interface (SEI) layer at the electrode surface.[8] In the first anodic scan, a relatively small peak located at 1.06 V, a broad peak at 1.47 V and a large peak at 2.1 V can be observed. The peaks at 1.06 and 1.47 V were related to the partial oxidation of Mo to MoS$_2$ owing to the defect sites, leading to the formation of MoS$_2$ (Equation 3)[8]; the peak at 2.1 V was associated with the oxidation of Li$_2$S into S (Equation 4).[32] In the subsequent cycles, a small peak emerged at 1.8 V in the cathodic scan, corresponding to the conversion reaction of S into Li$_2$S (Equation 5); the cathodic peaks located at 1.25 and 0.5 V were attributed to the lithium ions intercalated into the MoS$_2$ lattice and the reduction of MoS$_2$ into
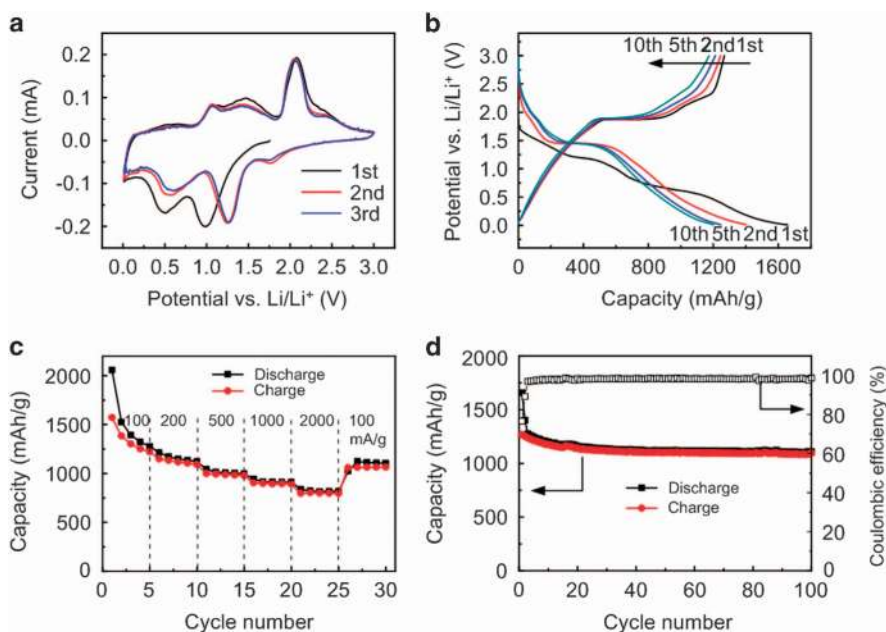
Figure 3 (a) CV curves of the MoS$_2$/VGNS nanostructural electrode of the first three cycles at a scan rate of 0.1 mV s^{-1} in a potential range of 0.01–3 V vs Li/Li$^+$. (b) Galvanostatic discharging/charging curves of the MoS$_2$/VGNS nanostructural electrode at a current density of 200 mA g^{-1} for the first 10 cycles. (c) Rate capability of MoS$_2$/VGNS nanocomposites from the current densities of 100–2000 mA g^{-1}. (d) Cycling performance and coulombic efficiency of MoS$_2$/VGNS at a current density of 200 mA g^{-1}. MoS$_2$ sample was grown with 11 mg of Mo salt precursor.

Mo nanoparticles, respectively.[33]

$$MoS_2 + xLi^+ + xe^- \rightarrow Li_xMoS_2 \tag{1}$$

$$Li_xMoS_2 + (4-x)Li^+ + (4-x)e^- \rightarrow Mo + 2Li_2S \tag{2}$$

$$Mo + 2Li_2S \rightarrow MoS_2 + 4Li^+ + 4e^- \tag{3}$$

$$Li_2S \rightarrow 2Li^+ + S + 2e^- \tag{4}$$

$$2Li^+ + S + 2e^- \rightarrow Li_2S \tag{5}$$

It is worth mentioning that unlike the MoS$_2$/VGNS nanocomposites, the peaks located at 0.5 V became indiscernible in the second and third cycles of the MoS$_2$/CB composites (Supplementary Figure S7a). This implied that the conversion reaction of MoS$_2$ into Mo nanoparticles was partially prevented in the MoS$_2$/CB composites after the first cycle, which was possibly due to the inferior electrical conductivity of MoS$_2$ and the ineffective ion transport in the MoS$_2$/CB nanostructure. It has been previously shown that the restacked thick MoS$_2$ layers during the cycling can indeed inhibit the conversion reaction via the reduced ion transport.[34] In fact, the same phenomenon was reported in a range of other dichalcogenide anode materials, where the peaks associated with conversion reactions disappeared after the first cycle.[1] In the present case, however, the direct integration of MoS$_2$ nano-leaves on the VGNS backbone can provide a multiscale 3D interconnected structure with facile electronic and ionic conductivity, which may significantly promote the conversion reaction and enhance the specific capacity of lithium storage.[8]

Figure 3b shows the galvanostatic discharge/charge curves for the first 10 cycles in the potential range of 0.01–3.0 V vs Li/Li$^+$ at a current density of 200 mA g^{-1}. In the first discharge curve, there are two plateaus located at 1.2–1.1 and 0.8–0.5 V. The former is ascribed to the formation of Li$_x$MoS$_2$ through lithium intercalation, and the latter is due to the conversion of MoS$_2$ into metallic Mo accompanied by the

formation of the SEI layer.[1,33] The MoS$_2$/VGNS nanocomposites also exhibited an obvious plateau in the potential range between 2.0 and 2.4 V in the first charge cycle, corresponding to the oxidization of Li$_2$S into S.[35] These discharge/charge behaviors are consistent with the CV curves shown in Figure 3a. Compared with the pristine VGNS and MoS$_2$/CB control samples (Supplementary Figures S6b and S7b), MoS$_2$/VGNS nanocomposites displayed longer flat plateaus, which may be attributed to the synergistic integration between MoS$_2$ and VGNS.

The specific capacities of the first lithiation/delithiation cycle were 1656 and 1268 mAh g^{-1}, respectively, calculated based on total mass of MoS$_2$ and VGNS. This resulted in an initial CE of 76.6%, which is among the best values reported in the recent literature.[8] A high initial CE is generally desirable for LIB because it means that a large portion of Li ions could be utilized in the subsequent cycles and indicates less consumption of cathode materials.[8] The high initial reversible lithium storage capability possibly arose from the unique MoS$_2$/VGNS nano-architectures, which provide a plethora of active sites act as Li-ion hosting sites.[35] In the second cycle, the discharge and charge capacities decreased to 1399 and 1244 mAh g^{-1}, respectively, corresponding to an increased CE of 88.9%. The value of CE further remained >96% for the subsequent cycles. These capacities were also notably higher than the theoretical value of MoS$_2$ calculated based on the conversion reaction, which may be due to the extra capacity contribution from the massive active sites that can accommodate additional Li ions by the vacancies, dislocations and distortions of MoS$_2$ nanostructures and VGNS backbones as pores, cavities or defect sites.[36] Nevertheless, further studies will be necessary to understand whether other mechanisms (for example, interfacial storage and electrolyte decomposition) also contributed to the electrochemical charge storage.[11]

The rate capability of MoS$_2$/VGNS nanostructures grown with various Mo salt precursors is shown in Figure 3c and Supplementary Figure S8a. The best rate capability was obtained from MoS$_2$/VGNS grown with 11 mg of Mo salt precursor. Reversible specific capacities of 1277, 1119, 996, 910 and 818 mAh g^{-1} were obtained at current

densities of 100, 200, 500, 1000 and 2000 mA g^{-1}, respectively (Figure 3c). Remarkably, the capacity returned to ~1104 mAh g^{-1} when the current density was adjusted from 2000 to 100 mA g^{-1}. By contrast, the specific capacity of MoS$_2$/VGNS grown with 3 mg of Mo salt precursor was much lower, ~718 and 374 mAh g^{-1} at current densities of 100 and 2000 mA g^{-1}, respectively (Supplementary Figure S8a). The low capacities at various current densities (especially at high current densities) of MoS$_2$/VGNS grown with 3 mg of Mo salt precursor were probably owing to the lower mass loading of MoS$_2$ (~0.19 mg cm^{-2}) as compared with that of MoS$_2$/VGNS grown with 11 mg of Mo salt precursor (~1.72 mg cm^{-2}). Although the specific capacity of MoS$_2$/VGNS grown with 22 mg of Mo salt precursor was relatively high at low current densities (for example, the specific capacity was 1109 mAh g^{-1} at a current density of 100 mA g^{-1}), it decayed much faster when the current density was increased (for example, the specific capacity was 495 mAh g^{-1} at a current density of 2000 mA g^{-1}). In addition, the MoS$_2$/CB control sample can deliver capacities of only 846 and 85 mAh g^{-1} at the current densities of 100 and 2000 mA g^{-1}, respectively (Supplementary Figure S7c), indicating that the structure of nanocomposites has had a critical role in the lithium-ion storage capability.

The rate capacity of MoS$_2$/VGNS nanostructures grown with 11 mg of Mo salt precursor is comparable to or better than the high-end values reported recently for many MoS$_2$-based hybrid anodes, particularly at a high current density (summarized in Supplementary Table S1). These results are attributed to the rationally designed multiscale submillimeter–submicron–nanometer architecture and the synergistic effect between MoS$_2$ and VGNS (Supplementary Figure S9). First, VGNS has outstanding electronic conductivity to improve the electron transfer rate.[19] Second, the vertically aligned VGNS can effectively inhibit the restacking of the MoS$_2$ layered structure and maintain its structure integrity. Third, given that lithium ions can effectively penetrate into the electrode and contact with active MoS$_2$ through submillimeter pores, lithiation and delithiation can be greatly facilitated in the nano-sized layered structure of MoS$_2$, which can provide a mass of active sites to enhance ion accessibility and shorten the path of Li diffusion.[26]

The cycling performance of MoS$_2$/VGNS nanocomposites is also shown in Figure 3d. Significantly, the electrode of MoS$_2$/VGNS grown with 11 mg of Mo salt precursors can deliver a capacity of 1109 mAh g^{-1} after 100 cycles at a current density of 200 mA g^{-1}, whereas the electrodes grown with 3 and 22 mg of Mo salt precursors
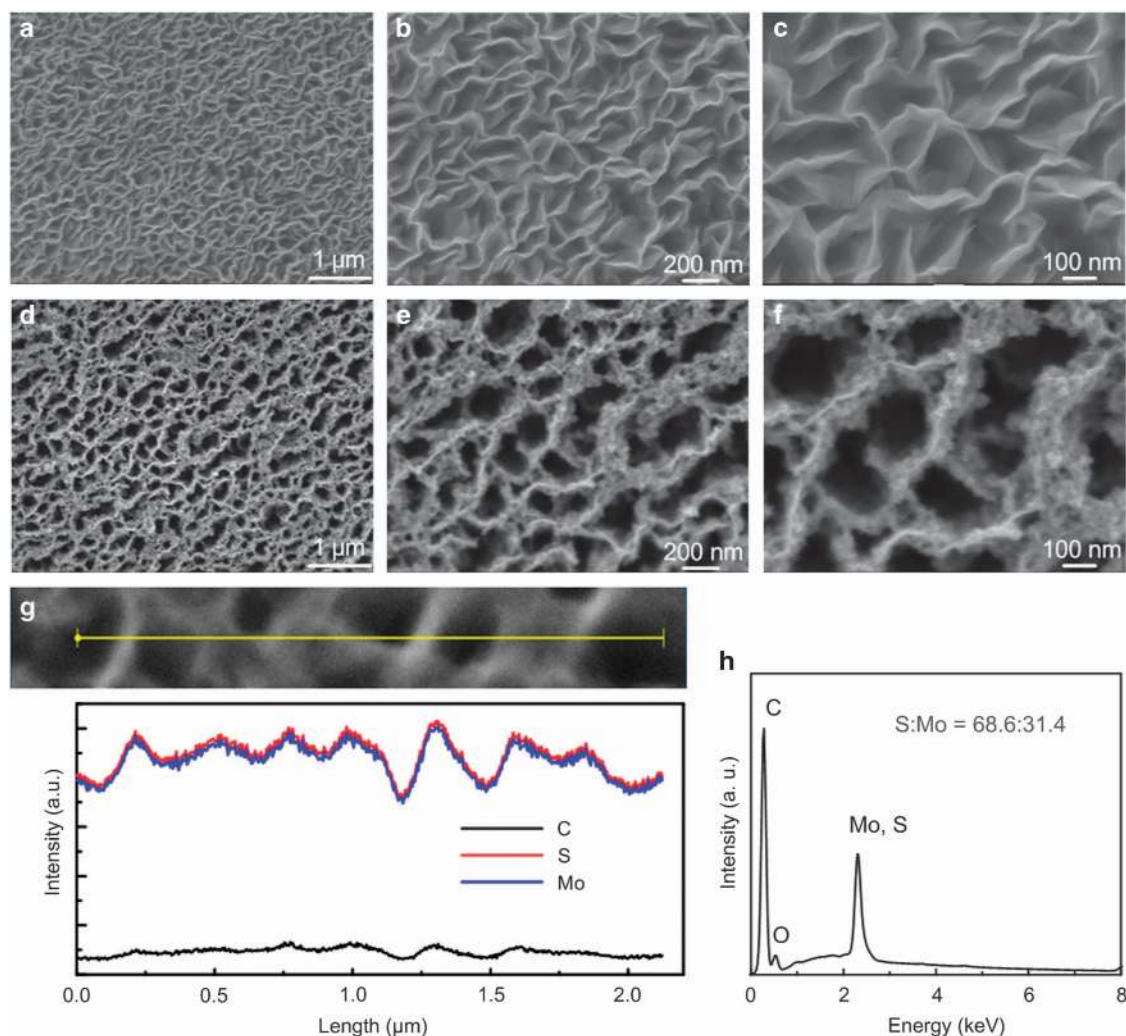
Figure 4 (**a–c**) Low- and high-magnification SEM images of pristine VGNS grown on graphite paper. (**d–f**) Low- and high-magnification SEM images of the MoS$_2$/VGNS nanostructures grown on graphite paper. (**g**) Line probe of elemental distributions of C, S and Mo on the top surface of MoS$_2$/VGNS. (**h**) EDX spectrum of MoS$_2$/VGNS. MoS$_2$ was grown with 110 mg of Mo salt precursor.
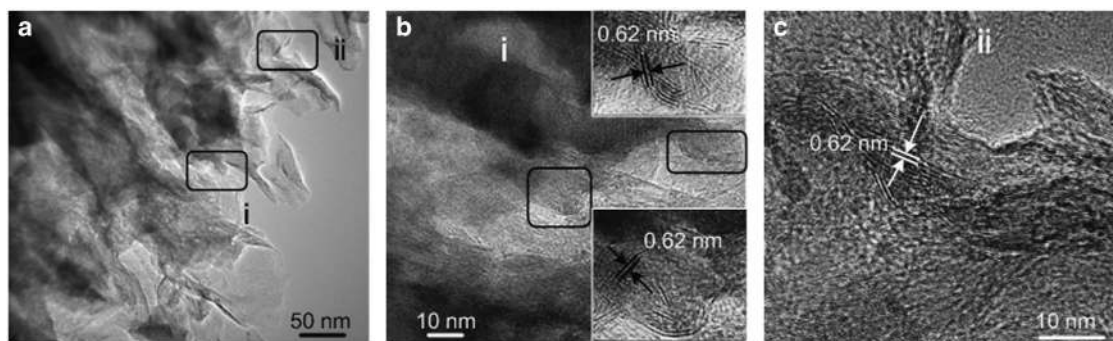
Figure 5 (**a**, **b**) TEM and (**c**) HRTEM images of MoS₂/VGNS grown on graphite paper. Insets in (**b**) show the lattice spacing of the (002) crystal plane of MoS₂.

can deliver capacities of 342 and 811 mAh g^{-1}, respectively (Supplementary Figure S8b). By contrast, the capacities of pure VGNS and MoS₂/CB control samples were much lower, ~127 and 186 mAh g^{-1} after 100 cycles at the same cycling conditions (Supplementary Figures S6d and S7d). Moreover, the MoS₂/VGNS (with 11 mg of Mo salt precursors) nanostructure maintained the original shape except that the MoS₂ nano-leaves shifted closer to VGNS backbones even after 100 cycles at a current density of 200 mA g^{-1} (Supplementary Figure S10), indicating stable and superior cycling performance. Again, the excellent cycling performance of MoS₂/VGNS nanocomposites can be attributed to the multiscale 3D structure because the stress generated upon lithiation was largely accommodated, and the size and dispersion characteristics of metallic Mo and Li₂S in the conversion reactions were stabilized by the supporting graphene nanosheets.[11]

To further explore the intrinsic electrochemical and kinetic mechanisms of MoS₂/VGNS, the EIS spectra were obtained after the first three cycles. Supplementary Figure S11 shows the Nyquist plots of pure VGNS, MoS₂/CB and MoS₂/VGNS nanocomposites grown with different amounts of Mo salt precursors. An equivalent circuit model was used to simulate the electrical components (inset of Supplementary Figure S11), where R_s represents the current collector and electrolyte resistance; R_f and CPE_1 are the SEI layer resistance and the constant-phase element (CPE), respectively; R_{ct} and CPE_2 are the charge transfer resistance and double-layer capacitor, respectively; and W is the Warburg impedance related to lithium diffusion.[37] The fitting results were summarized in Supplementary Table S2, which clearly shows that the charge transfer resistance of the MoS₂/VGNS electrode was significantly increased from 28.73 to 228.27 Ω when the amount of Mo salt precursor was increased from 3 to 22 mg. The highest charge transfer resistance was observed on the MoS₂/CB control sample, indicating the poor electrical conductivity of the system.

HER performance

Because hydrogen production requires an acidic environment and Ni becomes unstable in the acidic solution, graphite paper instead of Ni foam was used to support MoS₂/VGNS in the HER experiments. The SEM images of pristine VGNS and MoS₂/VGNS nanocomposites grown on graphite paper are shown in Figures 4a–f. One can see that the morphology of pristine VGNS was similar to that on Ni foam (Figure 1b), that is, maze-like VGNS networks with submicron cavities between neighboring graphene nanosheets. By contrast, the morphology of MoS₂/VGNS on graphite paper was significantly different from that on Ni foam. It was found that the MoS₂ nano-leaves were much shorter, and the growth rate was much slower (Supplementary Figure S12). A higher amount of Mo salt precursor at

110 mg was therefore needed to produce a similar mass loading of MoS₂ as in the case of Ni foam.

The EDX analysis was also performed to investigate the elemental distributions of Mo, S and C, as shown in Figures 4g and h. A probe line along the material surface clearly showed that the intensities of Mo and S changed synchronously and matched the profile of nanostructures in the SEM image. The intensities of Mo and S were much higher than that of C, indicating that MoS₂ uniformly coated the surface of VGNS. When the Mo salt precursor was reduced from 110 to 11 mg, the MoS₂ loading decreased correspondingly from 0.21 to 0.07 mg cm^{-2}, resulting in a higher signal of C as compared with Mo and S in the EDX line profiling (Supplementary Figure S13).

Figure 5 shows the TEM and HRTEM images of MoS₂/VGNS grown on graphite paper, where the size of MoS₂ nano-leaves was much smaller (10–20 nm) as compared with those on Ni foam (~50 nm), which in good agreement with the SEM observations. In addition, Raman spectra of the pure VGNS and MoS₂/VGNS on graphite paper were plotted in Supplementary Figure S14. The ratio of D-to-G peak intensities (I_D/I_G) in the Raman spectra was used to investigate the defect levels in the respective carbon nanostructures.[30] The I_D/I_G ratios were 1.38 and 0.96 for the pristine VGNS and graphite MoS₂/VGNS on graphite paper, respectively, indicating that the defects on VGNS were reduced after the solvothermal growth of MoS₂. The better graphitic structure was possibly due to the thermal healing effect during the synthesis.[38]

The electrocatalytic HER activities of the synthesized MoS₂/VGNS nanocomposites were then evaluated in a typical three-electrode configuration. Figures 6a and b shows the polarization curves and related parameters (onset potential and Tafel slope) for pure VGNS, MoS₂/VGNS and control samples of MoS₂/CB and MoS₂/CB mixed with VGNS grown on graphite paper. It is clearly seen that the MoS₂/VGNS nanocomposites had the highest current density (at a fixed voltage, for example, −0.3 V) (Figure 6a), the smallest Tafel slope and the lowest onset potential as compared with the pristine VGNS and the other two control samples (Figure 6b). The synthesized MoS₂/VGNS can achieve a small Tafel slope of 41.3 mV dec^{-1}, with the onset potential of −0.16 V. Furthermore, electrocatalytic HER activity is also determined by the electrochemical surface area of the electrode. The electrochemical surface area is directly proportional to the double-layer capacitance (C_{dl}), which is related to the double-layer current response in the cyclic voltammograms (Figure 6c and Supplementary Figure S15).[39] C_{dl} is estimated from the half value of the slope of the curve by plotting the difference between anodic and cathodic current densities at 0.3 V vs RHE against the scan rate (Figure 6d). The C_{dl} of MoS₂/VGNS is 7.96 mF cm^{-2}, which is approximately 20 times larger than that of MoS₂/CB (0.40 mF cm^{-2}),
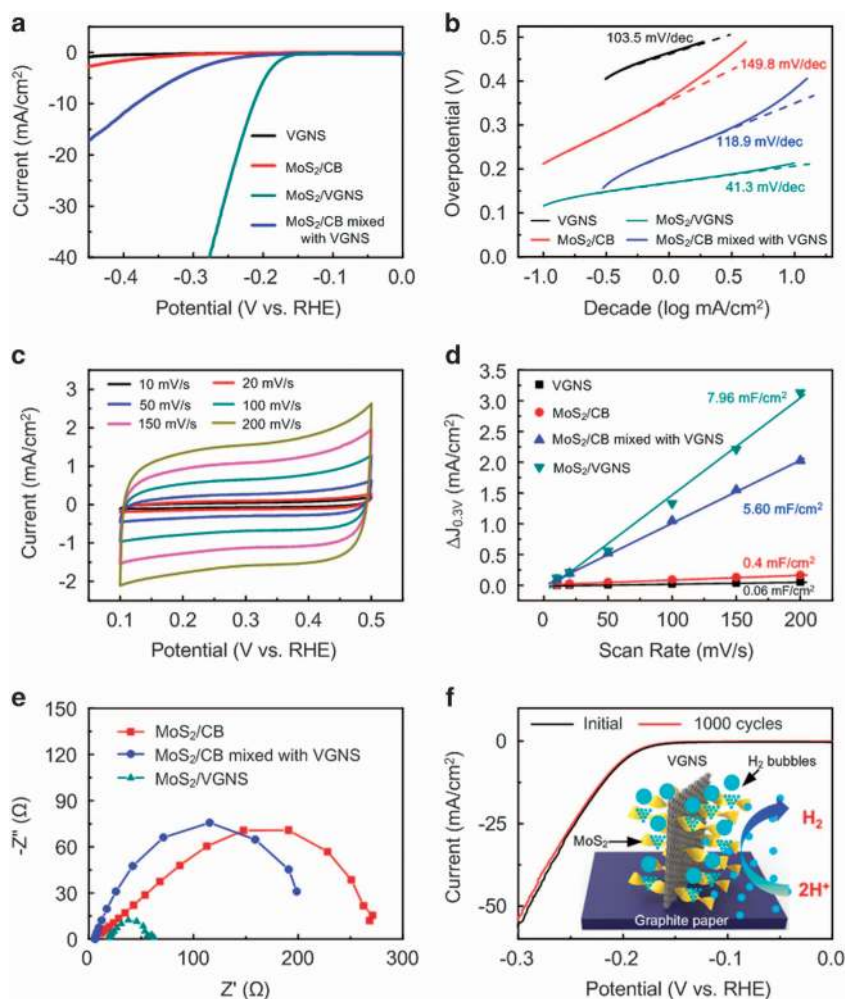
Figure 6 (**a**) Polarization and related (**b**) Tafel plot curves of MoS₂/VGNS, pure VGNS, MoS₂/CB and MoS₂/CB mixed with VGNS electrodes. (**c**) CV of MoS₂/VGNS electrode at various scan rates in a potential range of 0.1–0.5 V vs RHE. (**d**) Linear fitting of the differences between the anodic and cathodic current density (ΔJ) at 0.3 V vs RHE plotted against scan rates to estimate the double-layer capacitances of the active electrodes. (**e**) EIS of MoS₂/VGNS, MoS₂/CB and MoS₂/CB mixed with VGNS electrodes. (**f**) Stability measurement of MoS₂/VGNS electrode with initial polarization curve (black curve) and after 1000 cycles (red curve) at a scan rate of 100 mV s^{-1}. Inset in (**f**) is a schematic diagram to show the working principle of MoS₂/VGNS catalyst for HER. MoS₂ nano-leaves grown from VGNS surface provide abundant reactive edges for hydrogen generation.

133 times larger than that of VGNS (0.06 mF cm^{-2}) and larger than that of MoS₂/CB physical combined with VGNS (5.60 mF cm^{-2}). The small Tafel and large C_{dl} of MoS₂/VGNS nanocomposites are among the best values reported in recent MoS₂-based HER catalysts (Supplementary Table S3). EIS was carried out to investigate the electrode kinetic in the HER process as shown in Figure 6e. The related equivalent circuit model used for the fitting is shown in the inset of Figure 6e. The charge transfer resistance of MoS₂/VGNS is only 39.2 Ω, which is much smaller than that of MoS₂/CB (322.1 Ω) and MoS₂/CB mixed with VGNS (220.4 Ω) electrode. The HER cycle stability of MoS₂/VGNS nanocomposites was tested continuously for 1000 cycles between 0 and − 0.3 V vs RHE at a scan rate of 100 mV s^{-1}. As shown in Figure 6f, the synthesized MoS₂/VGNS electrode exhibits negligible loss even after 1000 cycles and maintains its electrocatalytic current density at 97.1% of its initial value, indicating long cycle stability performance.

The superior catalytic performance of MoS₂/VGNS nanocomposites for HER can be attributed to advantageous structural features and strong chemical and electronic coupling between MoS₂ nano-leaves and VGNS.[6,40] Compared with MoS₂/CB mixed with VGNS control

sample, MoS₂ is chemically grown on VGNS for MoS₂/VGNS electrode instead of simple physical contact with VGNS (MoS₂/CB mixed with VGNS sample), which allows the charges generated during the HER process to quickly transfer to VGNS. Moreover, because the nanocomposites contained a high density of microscale cavities and nanoscale pores, the electrolyte can easily access the active sites of MoS₂ nano-leaves to produce hydrogen. At the same time, smaller MoS₂ nano-leaves possessed abundant reactive edges, which have been demonstrated to be highly catalytically active for hydrogen generation.[6] Finally, the structural integrity between VGNS and MoS₂ nano-leaves can provide good electronic transport to further enhance the electrochemical catalytic performance (inset in Figure 6f).

CONCLUSION
In summary, MoS₂ nano-leaves were successfully grown on VGNS to form MoS₂/VGNS hybrid nanostructures by a simple solvothermal method, and their application as the anode material of LIBs and the electrodes of HER was demonstrated. The MoS₂/VGNS nanostructures delivered a specific capacity of 1277 mAh g^{-1} at a current density of 100 mA g^{-1} with a high initial CE of 76.6%.

Moreover, the MoS$_2$/VGNS nanostructures acted as the catalysts for HER, with a minimal Tafel slope of 41.3 mV dec^{-1}. The excellent performance of MoS$_2$/VGNS in LIB and HER applications was related to the rationally designed multiscale architecture and the synergistic effect between MoS$_2$ and VGNS, which displayed merits such as large surface area, good electronic conductivity, short Li diffusion path, enhanced ion accessibility and stable structural integrity. Our results may open up a new avenue for the development of MoS$_2$-based structures with multifunctions for a variety of applications.

CONFLICT OF INTEREST

The authors declare no conflict of interest.

1 Shi, Y., Wang, Y., Wong, J. I., Tan, A. Y. S., Hsu, C.-L., Li, L.-J., Lu, Y. C. & Yang, H. Y. Self-assembly of hierarchical MoS$_x$/CNT nanocomposites (2<x<3): towards high performance anode materials for lithium ion batteries. *Sci. Rep.* **3**, 2169 (2013).

2 Shi, Y., Zhou, W., Lu, A.-Y., Fang, W., Lee, Y.-H., Hsu, A. L., Kim, S. M., Kim, K. K., Yang, H. Y., Li, L. J., Idrobo, J. C. & Kong, J. van der Waals epitaxy of MoS$_2$ layers using graphene as growth templates. *Nano Lett.* **12**, 2784–2791 (2012).

3 Radisavljevic, B., Radenovic, A., Brivio, J., Giacometti, V. & Kis, A. Single-layer MoS$_2$ transistors. *Nat. Nanotechnol.* **6**, 147–150 (2011).

4 Sundaram, R. S., Engel, M., Lombardo, A., Krupke, R., Ferrari, A.C., Avouris, P. & Steiner, M. Electroluminescence in single layer MoS$_2$. *Nano Lett.* **13**, 1416–1421 (2013).

5 Wang, L., Wang, Y., Wong, J. I., Palacios, T., Kong, J. & Yang, H. Y. Functionalized MoS$_2$ nanosheet-based field-effect biosensor for label-free sensitive detection of cancer marker proteins in solution. *Small* **10**, 1101–1105 (2014).

6 Li, Y. G., Wang, H. L., Xie, L. M., Liang, Y. Y., Hong, G. S. & Dai, H. J. MoS$_2$ nanoparticles grown on graphene: an advanced catalyst for the hydrogen evolution reaction. *J. Am. Chem. Soc.* **133**, 7296–7299 (2011).

7 Liu, H., Su, D., Zhou, R., Sun, B., Wang, G. & Qiao, S. Z. Highly ordered mesoporous MoS$_2$ with expanded spacing of the (002) crystal plane for ultrafast lithium ion storage. *Adv. Energy Mater.* **2**, 970–975 (2012).

8 Wang, J., Liu, J., Chao, D., Yan, J., Lin, J. & Shen, Z. X. Self-assembly of honeycomb-like MoS$_2$ nanoarchitectures anchored into graphene foam for enhanced lithium-ion storage. *Adv. Mater.* **26**, 7162–7169 (2014).

9 Zhu, C., Mu, X., van Aken, P. A., Yu, Y. & Maier, J. Single-layered ultrasmall nanoplates of MoS$_2$ embedded in carbon nanofibers with excellent electrochemical performance for lithium and sodium storage. *Angew. Chem. Int. Ed.* **53**, 2152–2156 (2014).

10 Zhu, C., Mu, X., van Aken, P. A., Maier, J. & Yu, Y. Fast Li storage in MoS$_2$-graphene-carbon nanotube nanocomposites: advantageous functional integration of 0D, 1D, and 2D nanostructures. *Adv. Energy Mater.* **5**, 1401170 (2015).

11 Xu, X., Liu, W., Kim, Y. & Cho, J. Nanostructured transition metal sulfides for lithium ion batteries: progress and challenges. *Nano Today* **9**, 604–630 (2014).

12 Stephenson, T., Li, Z., Olsen, B. & Mitlin, D. Lithium ion battery applications of molybdenum disulfide (MoS$_2$) nanocomposites. *Energy Environ. Sci.* **7**, 209–231 (2014).

13 Chang, Y. H., Lin, C. T., Chen, T. Y., Hsu, C. L., Lee, Y. H., Zhang, W., Wei, K. H. & Li, L. J. Highly efficient electrocatalytic hydrogen production by MoS$_x$ grown on graphene-protected 3D Ni foams. *Adv. Mater.* **25**, 756–760 (2013).

14 Zheng, X., Xu, J., Yan, K., Wang, H., Wang, Z. & Yang, S. Space-confined growth of MoS$_2$ nanosheets within graphite: the layered hybrid of MoS$_2$ and graphene as an active catalyst for hydrogen evolution reaction. *Chem. Mater.* **26**, 2344–2353 (2014).

15 Chang, K. & Chen, W. l-Cysteine-assisted synthesis of layered MoS$_2$/graphene composites with excellent electrochemical performances for lithium ion batteries. *ACS Nano* **5**, 4720–4728 (2011).

16 Cao, X., Shi, Y., Shi, W., Rui, X., Yan, Q., Kong, J. & Zhang, H. Preparation of MoS$_2$-coated three-dimensional graphene networks for high-performance anode material in lithium-ion batteries. *Small* **9**, 3433–3438 (2013).

17 Smith, A. J., Chang, Y. H., Raidongia, K., Chen, T. Y., Li, L. J. & Huang, J. Molybdenum sulfide supported on crumpled graphene balls for electrocatalytic hydrogen production. *Adv. Energy Mater.* **4**, 1400398 (2014).

18 Seo, D. H., Han, Z. J., Kumar, S. & Ostrikov, K. K. Structure-controlled, vertical graphene-based, binder-free electrodes from plasma-reformed butter enhance supercapacitor performance. *Adv. Energy Mater.* **3**, 1316–1323 (2013).

19 Han, Z. J., Seo, D. H., Yick, S., Chen, J. H. & Ostrikov, K. K. MnO$_x$/carbon nanotube/ reduced graphene oxide nanohybrids as high-performance supercapacitor electrodes. *NPG Asia Mater.* **6**, e140 (2014).

20 El-Kady, M. F., Strong, V., Dubin, S. & Kaner, R. B. Laser scribing of high-performance and flexible graphene-based electrochemical capacitors. *Science* **335**, 1326–1330 (2012).

21 Yang, X., Zhu, J., Qiu, L. & Li, D. Bioinspired effective prevention of restacking in multilayered graphene films: towards the next generation of high-performance super-capacitors. *Adv. Mater.* **23**, 2833–2838 (2011).

22 Cheng, Y., Lu, S., Zhang, H., Varanasi, C. V. & Liu, J. Synergistic effects from graphene and carbon nanotubes enable flexible and robust electrodes for high-performance supercapacitors. *Nano Lett.* **12**, 4206–4211 (2012).

23 Thakur, M., Sinsabaugh, S. L., Isaacson, M. J., Wong, M. S. & Biswal, S. L. Inexpensive method for producing macroporous silicon particulates (MPSPs) with pyrolyzed polyacrylonitrile for lithium ion batteries. *Sci. Rep.* **2**, 795 (2012).

24 Seo, D. H., Yick, S., Pineda, S., Su, D., Wang, G., Han, Z. J. & Ostrikov, K. K. Single-step, plasma-enabled reforming of natural precursors into vertical graphene electrodes with high areal capacitance. *ACS Sustainable Chem. Eng.* **3**, 544–551 (2015).

25 Wu, Z.-S., Zhou, G., Yin, L.-C., Ren, W., Li, F. & Cheng, H.-M. Graphene/metal oxide composite electrode materials for energy storage. *Nano Energy* **1**, 107–131 (2012).

26 Liu, C., Li, F., Ma, L. P. & Cheng, H. M. Advanced materials for energy storage. *Adv. Mater.* **22**, E28–E62 (2010).

27 Hwang, H., Kim, H. & Cho, J. MoS$_2$ nanoplates consisting of disordered graphene-like layers for high rate lithium battery anode materials. *Nano Lett.* **11**, 4826–4830 (2011).

28 Li, H., Zhang, Q., Yap, C. C. R., Tay, B. K., Edwin, T. H. T., Olivier, A. & Baillargeat, D. From bulk to monolayer MoS$_2$: evolution of Raman scattering. *Adv. Funct. Mater.* **22**, 1385–1390 (2012).

29 Zhang, X., Han, W., Wu, J., Milana, S., Lu, Y., Li, Q., Ferrari, A. C. & Tan, P. H. Raman spectroscopy of shear and layer breathing modes in multilayer MoS$_2$. *Phys. Rev. B* **87**, 115413 (2013).

30 Ferrari, A., Meyer, J., Scardaci, V., Casiraghi, C., Lazzeri, M., Mauri, F., Piscanec, S., Jiang, D., Novoselov, K. S., Roth, S. & Geim, A. K. Raman spectrum of graphene and graphene layers. *Phys. Rev. Lett.* **97**, 187401 (2006).

31 Eigler, S. & Hirsch, A. Chemistry with graphene and graphene oxide—challenges for synthetic chemists. *Angew. Chem. Int. Ed.* **53**, 7720–7738 (2014).

32 Xiao, J., Wang, X., Yang, X.Q., Xun, S., Liu, G., Koech, P.K., Liu, J. & Lemmon, J. P. Electrochemically induced high capacity displacement reaction of PEO/MoS$_2$/graphene nanocomposites with lithium. *Adv. Funct. Mater.* **21**, 2840–2846 (2011).

33 Wang, Z., Chen, T., Chen, W., Chang, K., Ma, L., Huang, G., Chen, D. & Lee, J. Y. CTAB-assisted synthesis of single-layer MoS$_2$-graphene composites as anode materials of Li-ion batteries. *J. Mater. Chem. A* **1**, 2202–2210 (2013).

34 Wang, P.-p., Sun, H., Ji, Y., Li, W. & Wang, X. Three-dimensional assembly of single-layered MoS$_2$. *Adv. Mater.* **26**, 964–969 (2014).

35 Zhou, J., Qin, J., Zhang, X., Shi, C., Liu, E., Zhao, N. & He, C. 2D space-confined synthesis of few-layer MoS$_2$ anchored on carbon nanosheet for lithium-ion battery anode. *ACS Nano* **9**, 3837–3848 (2015).

36 Chang, K., Geng, D., Li, X., Yang, J., Tang, Y., Cai, M., Li, R. & Sun, X. Ultrathin MoS$_2$/ nitrogen-doped graphene nanosheets with highly reversible lithium storage. *Adv. Energy Mater.* **3**, 839–844 (2013).

37 Wang, Y., Han, Z. J., Yu, S. F., Song, R. R., Song, H. H., Ostrikov, K. K. & Yang, H. Y. Core-leaf onion-like carbon/MnO$_2$ hybrid nano-urchins for rechargeable lithium-ion batteries. *Carbon* **64**, 230–236 (2013).

38 Cao, A., Liu, Z., Chu, S., Wu, M., Ye, Z., Cai, Z., Chang, Y., Wang, S., Gong, Q. & Liu, Y. A facile one-step method to produce graphene–CdS quantum dot nanocomposites as promising optoelectronic materials. *Adv. Mater.* **22**, 103–106 (2010).

39 Lukowski, M. A., Daniel, A. S., Meng, F., Forticaux, A., Li, L. & Jin, S. Enhanced hydrogen evolution catalysis from chemically exfoliated metallic MoS$_2$ nanosheets. *J. Am. Chem. Soc.* **135**, 10274–10277 (2013).

40 Xiang, Q., Yu, J. & Jaroniec, M. Synergetic effect of MoS$_2$ and graphene as cocatalysts for enhanced photocatalytic H$_2$ production activity of TiO$_2$ nanoparticles. *J. Am. Chem. Soc.* **134**, 6575–6578 (2012).

Supplementary Information accompanies the paper on the NPG Asia Materials website (http://www.nature.com/am)